The Circulation Associated with a Cold Front. Part II: Moist Case

B. B. ROSS AND I. ORLANSKI

Geophysical Fluid Dynamics Laboratory/NOAA, Princeton University, Princeton 08540

(Manuscript received 10 June 1977, in final form 27 October 1977)

ABSTRACT

The effect of moisture upon the dynamics of mature idealized cold front systems is investigated using a two-dimensional numerical model. Lifting produced by the initial cross-stream frontal circulation studied by Orlanski and Ross (1977) is shown to saturate the warm moist air above the nose of the front when initial humidity levels are sufficiently high. If the atmosphere is convectively unstable, this saturated air will develop into deep convection with the convection-induced circulation overwhelming the initial frontal circulation. The initial development of convection is also shown to produce a gravity wave exhibiting similar scales to those of the convective zone. This wave propagates into the warm air at a much faster speed than the moving front-cloud system. Comparisons are made of the intensity of convection for different initial humidity and temperature conditions and when a low-level capping inversion is present. Also a comparison is made of cloud development caused by a combination of frontal lifting and surface heating when temperature inversions of different intensities are present. The stronger inversion is shown to suppress convection produced by surface heating alone with the combined effect of frontal lifting and surface heating required to release the convective instability.

1. Introduction

The generation of a cross-stream circulation by a mature two-dimensional frontal system was investigated by Orlanski and Ross (1977) for dry atmospheric conditions. The numerical solutions produced in that study (which we will refer to as "Part I") exhibited ageostrophic two-dimensional rolls aligned along the front which were shown to be determined by the large-scale wind gradients within the frontal region. The lifting produced by these rolls is considered by meteorologists as the primary mechanism for initiating the convective activity which often accompanies a moving cold front. A basic question to be considered in the present paper is how the inclusion of moist processes will alter the dry frontal circulation.

An important aspect of the frontal system including moisture is the large difference in scales which develops as the frontal circulation produces convective clouds with horizontal scales of the order of 1–10 km. Present numerical models are not capable of resolving both cloud-scale phenomena and frontal-scale dynamics in the same model. Cornelius *et al.* (1975) have investigated the inclusion of moisture in the steady-state front solutions of Williams (1974); they employ a convective adjustment scheme in their two-dimensional model to prevent unresolved moist convection from destroying their numerical solutions. In the present study, we will take an alternate approach in which we will not adjust the unstable atmosphere to a neutral lapse rate at each time step but will employ an eddy viscosity which becomes very large in moist unstable regions. As a result, the unstable convective zones which would consist of a group of cumulus clouds in the real atmosphere will develop as large-scale "clouds" in the present model which evolve in time as the atmospheric instability is released. These convective systems will be treated here as large-scale representations of the aggregate of cumulus clouds for the purpose of considering the two-way interaction between the frontal system and the convective activity. In particular, comparisons will be made of various features such as maximum vertical velocity and final cloud-top height for different sets of large-scale conditions. These comparisons can then be used to determine which conditions will produce the most intense convective activity in real atmospheric fronts. In studying this interaction, we will consider changes in initial humidity and temperature magnitudes as well as the inclusion of more realistic features such as a low-level temperature inversion, diurnally varying surface heating, and horizontal variation of relative humidity.

In Section 2, we will describe alterations which have been made to the dry model of Part I to accommodate moisture and moist processes. In Section 3, we will discuss the changes in the frontal circulation in the presence of moisture. A description of the resulting moist convection will be presented together with a discussion of the large-scale gravity waves which the

0022-4928/78/0445-0465$10.50

initial convective activity produces. The sensitivity of the moist solutions to changes in initial humidity and temperature levels will be discussed in Section 4. More complex frontal solutions will be described in Section 5 in which a low-level temperature inversion, diurnally varying surface heating, and more realistic initial conditions are included. Finally conclusions will be presented in Section 6.

2. Description of the model

The numerical model used in the present study is the same as that of Part I but with the inclusion of water vapor and condensed water together with the associated moist thermodynamic and dynamic processes. It is a two-dimensional finite-difference model in which variables are assumed to be constant in the y-direction along the axis of the front (with the exception of a potential temperature gradient which maintains the mean geostrophic balance). The model is 15 km deep with a rigid lid at the top ($z=H$); the tropopause is located at 10 km height. Coordinate stretching is used in z to increase the number of points near the ground (Δz is 145 m at the ground and increases to 400 m at $z=H$). The domain is 1500 km long with open boundaries at the ends ($x=0$, L). The model contains 51 points in the vertical and 76 points in the horizontal. The resulting horizontal grid size Δx is 20 km. The normal time increment Δt is 60 s.

In the present section, we will confine our discussion to changes and additions to the model of Part I.

a. Formulation of equations

The only change in the momentum equations is in the buoyancy term of the equation for vorticity $\zeta \equiv u_z - w_x$. This change, which is underlined in the equations which follow, results from the positive buoyancy of water vapor and the negative buoyancy of liquid water:

$$\frac{\partial \zeta}{\partial t} - J(\psi, \alpha_0 \zeta) = f\frac{\partial v}{\partial z} - g\frac{\partial}{\partial x}\left[\frac{\theta}{\Theta_0} + \underline{0.001(0.608q - c)}\right] + \frac{\partial}{\partial x}\left(K\nu_e\frac{\partial \zeta}{\partial x}\right) + \frac{\partial}{\partial z}\left(\nu_e\frac{\partial \zeta}{\partial z}\right) \quad (2.1)$$

$$\frac{\partial v}{\partial t} - \alpha_0 J(\psi, v) = -f\left(\alpha_0\frac{\partial \psi}{\partial z} - U_g\right) + \frac{\partial}{\partial x}\left(K\nu_e\frac{\partial v}{\partial x}\right) + \frac{\partial}{\partial z}\left(\nu_e\frac{\partial v}{\partial z}\right). \quad (2.2)$$

The quantities q and c are the water vapor and condensed water mixing ratios (g kg^{-1}) respectively. The factor 0.001 in the buoyancy term is needed to make the mixing ratios dimensionless.

The fundamental diagnostic relation between vorticity ζ and streamfunction ψ is the second-order elliptic equation

$$\zeta = \alpha_0\frac{\partial^2 \psi}{\partial x^2} + \frac{\partial}{\partial z}\left(\alpha_0\frac{\partial \psi}{\partial z}\right). \quad (2.3)$$

In the dry solutions of Part I, it was possible to make the hydrostatic approximation, in which the x-derivative on the right-hand side of (2.3) is neglected to obtain the much simpler relation

$$\zeta = \frac{\partial}{\partial z}\left(\alpha_0\frac{\partial \psi}{\partial z}\right). \quad (2.4)$$

This could be done because the horizontal scales in the dry frontal circulation were two orders of magnitude larger than the vertical scales. On the other hand, when moist convection takes place, one may expect that horizontal and vertical scales will be comparable and that Eq. (2.3) must therefore be used. In the present case, however, because of the large horizontal mesh size of 20 km which is required to resolve frontal-scale phenomena, the horizontal scales of motion in moist convective regions are still restricted to be at least an order of magnitude larger than vertical scales.

In order to determine the sensitivity of the moist model to our choice of streamfunction-vorticity equation, we have produced three test solutions for a typical frontal case involving moist convection. These cases were all identical except for the procedure for determining stream function from vorticity: one solution uses the full equation (2.3), the second uses the hydrostatic equation (2.4), and the third uses equation (2.4) followed by a horizontal filter to remove the highest wavenumber noise in x. The results of this comparison, as described in the Appendix, show little difference between the basic hydrostatic and anelastic results. The hydrostatic method with filtering shows very similar results to the first two methods during the initial stages of cloud development but with the filtered solution exhibiting reduction in the peak convective vertical velocity as well as the amplitude of high wavenumber gravity waves generated by the convection. Because moist convection is only crudely simulated by the model, we feel that the simpler hydrostatic equation with filtering is acceptable; we will therefore use it in the solutions to be presented in subsequent sections.

The fundamental change in the present model is the inclusion of conservation equations for water vapor and condensed water and the accompanying source term in the thermodynamic equation for latent heat release. Because of the inability of the model to resolve detailed cloud structure due to the present horizontal resolution, it was felt to be inappropriate to include a rain water

or frozen water phase. In the case of rain water, the approach to be taken here is that any condensed water amount in excess of a threshold value of 1.5 g kg^{-1} would be irreversibly removed from the atmosphere. [The procedure of converting condensed water in excess of a prescribed amount to rain droplets was used by Takeda (1965) and others.]

The primary mechanism of interest in the moisture budget is the treatment of phase changes between vapor and liquid states. We assume in the model that any water vapor in excess of an effective saturation mixing ratio kq_s immediately condenses, where $k \leqslant 1$. The factor k, which will be set to 0.95 here, is included in the condensation scheme in view of the fact that the mixing ratio q at each grid point is averaged over a 20 km wide box and begins to condense when the average relative humidity over this box is less than 100%.[1]

The method used in computing the water condensed or evaporated in one time step must account for the feedback effect which the temperature change due to latent heat release has upon the saturation mixing ratio q_s (Asai, 1962). The procedure (Lipps, 1977) used here is described below and is similar to the scheme presented by Takeda (1971):

1) Tentative values of potential temperature θ' and moisture quantities q' and c' are obtained for the time $t+\Delta t$ with the assumption that no condensation or evaporation takes place. Thus with leap-frog time differencing, the equations may be written

$$\theta'(t+\Delta t)=\theta(t-\Delta t)+2\Delta t\Big[\alpha_0 J(\psi,\theta)+v\frac{\partial\theta_0}{\partial y}+\frac{\partial}{\partial x}\Big(K\kappa_e\frac{\partial\theta}{\partial x}\Big)+\frac{\partial}{\partial z}\Big(\kappa_e\frac{\partial\theta}{\partial z}\Big)\Big], \quad (2.5)$$

$$q'(t+\Delta t)=q(t-\Delta t)+2\Delta t\Big[\alpha_0 J(\psi,q)+\frac{\partial}{\partial x}\Big(K\kappa_e\frac{\partial q}{\partial x}\Big)+\frac{\partial}{\partial z}\Big(\kappa_e\frac{\partial q}{\partial z}\Big)\Big], \quad (2.6)$$

$$c'(t+\Delta t)=c(t-\Delta t)+2\Delta t\Big[\alpha_0 J(\psi,c)+\frac{\partial}{\partial x}\Big(K\kappa_e\frac{\partial c}{\partial x}\Big)+\frac{\partial}{\partial z}\Big(\kappa_e\frac{\partial c}{\partial z}\Big)\Big], \quad (2.7)$$

[1] The value $k=0.95$ was taken as a compromise between the limit $k=1$ when the grid size goes to zero and the value $k=0.80$ used by Miyakoda *et al.* (1969) (involving a hemispheric model of the general circulation with 270 km grid spacing in midlatitudes). As observed by Miyakoda *et al.* and earlier by Smagorinsky (1960), the quantity k will depend upon the environmental conditions under which the condensation takes place in addition to the grid size of the model.

where quantities not followed by the time in brackets are evaluated at time t.

2) We define $\theta^*(t+\Delta t)$ and $q_s^*(t+\Delta t)$ to be tentative values for the potential temperature and saturation mixing ratio at $t+\Delta t$ if a phase change does occur. Then

$$\theta^*(t+\Delta t)=\theta'(t+\Delta t)+\frac{L}{c_p\pi_0}[q'(t+\Delta t)-kq_s^*(t+\Delta t)]. \quad (2.8)$$

Also under the anelastic approximation of Ogura and Phillips (1962), the saturation mixing ratio is expressed as

$$q_s=q_{s0}\exp\Big(\frac{L}{R_vT_0^2}\pi_0\theta\Big),$$

where quantities with the subscript "0" are mean-state values. The leap-frog finite-difference approximation to the time derivative of this expression is

$$q_s^*(t+\Delta t)-q_s(t-\Delta t)=q_s\frac{L\pi_0}{R_vT_0^2}[\theta^*(t+\Delta t)-\theta(t-\Delta t)] \quad (2.9)$$

where q_s is evaluated at time t. Substituting (2.9) into (2.8) to eliminate $q_s^*(t+\Delta t)$ and solving for $\theta^*(t+\Delta t)$, we obtain

$$\theta^*(t+\Delta t)=\theta(t-\Delta t)+\Big\{\theta'(t+\Delta t)-\theta(t-\Delta t)+\frac{L}{c_p\pi_0}\Big[q'(t+\Delta t)-kq_s(t-\Delta t)\Big]\Big\}\Big/\Big(1+\frac{L^2q_s}{c_pR_vT_0^2}k\Big). \quad (2.10)$$

3) With $\theta^*(t+\Delta t)$ determined, $q_s^*(t+\Delta t)$ is determined from (2.9); it is then possible to compute the phase change δ^* appropriate for the intermediate values θ^* and q_s^* at $t+\Delta t$, namely:

$$\delta^*(t+\Delta t)=q'(t+\Delta t)-kq_s^*(t+\Delta t).$$

The actual phase change δ will be determined according to the conditions

$$\delta=\begin{cases}0, & \text{if } \delta^*\leqslant 0 \text{ and } c'(t+\Delta t)=0\\ \delta^*, & \text{if } \delta^*>0 \text{ (condensation)}\\ \delta^*, & \text{if } -c'(t+\Delta t)<\delta^*<0 \text{ (partial evaporation)}\\ -c'(t+\Delta t), & \text{if } \delta^*<0 \text{ and } |\delta^*|\geqslant c'(t+\Delta t)>0 \text{ (complete evaporation).}\end{cases} \quad (2.11)$$

If $c'(t+\Delta t)$ is not permitted to be negative, these conditions can be summarized as

$$\delta=\max[\delta^*,\ -c'(t+\Delta t)]. \quad (2.11')$$

4) The final values of θ, q, and c at $t+\Delta t$ are then computed as

$$\left.\begin{aligned}\theta(t+\Delta t)&=\theta'(t+\Delta t)+\frac{L}{c_p\pi_0}\delta\\ q(t+\Delta t)&=q'(t+\Delta t)-\delta\\ c(t+\Delta t)&=c'(t+\Delta t)+\delta\end{aligned}\right\}, \tag{2.12}$$

where q and c are required to be non-negative.

The eddy viscosity formulation to be used here is adapted from the formulation first used by Orlanski and Ross (1973). The viscosity treatment in that paper involved a constant background viscosity υ_0 and a non-linear term which was only non-zero at points where the stratification was unstable, i.e., $\theta_z<0$.

In this paper, we will employ the equivalent potential temperature gradient θ_{e_z} when extending the viscosity formulation to the moist case, where

$$\theta_e=\theta\exp\left(\frac{Lkq_s}{c_p\pi_0\theta}\right).$$

Hence, the viscosity will be determined by the potential temperature gradient θ_z when the air is unsaturated and by the equivalent potential temperature gradient θ_{e_z} when saturation occurs. Because of this dependence upon θ_z and θ_{e_z}, the viscosity formulation produces strong diffusive effects in regions which are statically unstable. In this way its effect is similar to that of convective adjustment procedures (Manabe *et al.*, 1965) which are frequently used in large-scale atmospheric models. However, because the present viscosity approach requires a number of time steps to adjust the unstable regions, it is considered to be more appropriate for mesoscale models than the usual "instantaneous" convective adjustment methods.

The eddy viscosity formulation to be used here is summarized as follows:

$$\upsilon_e=\begin{cases}\upsilon_0, & \text{if } q<kq_s \text{ and } \Delta\theta\geqslant 0 \text{ or } q=kq_s \text{ and } \Delta\theta_e\geqslant 0\\ \upsilon_0\left\{1+C\left[\left(\dfrac{g|\Delta\theta|(\Delta z)^3}{\Theta_{0\kappa_0\upsilon_0}}\right)^{\frac{1}{2}}\right]\right\}, & \\ & \text{if } q<kq_s \text{ and } \Delta\theta<0\\ \upsilon_0\left\{1+C\left[\left(\dfrac{g|\Delta\theta_e|(\Delta z)^3}{\Theta_{0\kappa_0\upsilon_0}}\right)^{\frac{1}{2}}\right]\right\}, & \\ & \text{if } q=kq_s \text{ and } \Delta\theta_e<0,\end{cases} \tag{2.13}$$

where $\Delta\theta$ and $\Delta\theta_e$ are local vertical grid-point differences. In the moist model, $\upsilon_e=0.7\,\kappa_e$ and $\upsilon_0=0.7\,\kappa_0$. The constant K included in the horizontal diffusion terms of the prognostic equations has a value of 400. Usual values of κ_0 and C are 5 m^2 s^{-1} and 1.00, although these quantities will be changed as noted in the text.

b. Boundary and initial conditions

The boundary conditions[2] in the model are unchanged from Part I except for the additional conditions required for moisture variables q and c:

$$q_z=c_z=0 \quad \text{at} \quad z=0,$$
$$q_{zz}=c_z=0 \quad \text{at} \quad z=H.$$

The one exception to these conditions is noted near the end of Section 3 where q at the surface is fixed at a prescribed relative humidity distribution $R(x)$ so that

$$q=q_sR(x) \quad \text{at} \quad z=0.$$

The values for q and c on the end boundaries $x=0$ and $x=L$ are obtained using the same open boundary conditions as in Part I but with the potential temperature phase velocity used in place of the separately computed phase velocities for q and c.

The moist solutions all will be started without moisture for some initial adjustment period in which the dry solution is allowed to develop an ageostrophic circulation. These solutions thus will be similar to cases which were studied in Part I. Water vapor will be added to the dry solution at time t_m (either 5 or 10 h). The procedure used here is to prescribe a water vapor mixing ratio q at each point and in the two time levels t_m and $t_m-\Delta t$ by imposing a given relative humidity distribution $R(x,z)$ over the model domain. In the initial cases to be discussed, this distribution R will only be a function of z; in these cases, R will be a piecewise-linear function of z with the following reference points: $R=80\%$ at $z=0$, $R=90\%$ at $z=2000$ m, $R=40\%$ at the top of the model, $z=15\,000$ m. Later, distributions will be used which change the relative humidity profiles by constant factors so that the R value at 2000 m will be reduced from 90% to 80% or 70%. The final cases involving both x and z variation in R will be detailed in Section 3.

3. Moisture effects on the frontal circulation

The effect of moisture upon the frontal circulation will be described here in the context of the two idealized front-jet configurations which were treated in Part I, namely, a surface jet (denoted by "SJ3" to be consistent with its designation in Part I) and a midtropospheric jet (denoted by "MTJ2"). It was shown in the previous paper that a positive wind shear U_z of the mean x-component of wind will initially produce different cross-stream circulation depending upon the sign and magnitude of the horizontal gradient of the y-velocity v. In addition, it was shown that, as the circulations approach an approximate steady state, the qualitative differences between the two configurations

[2] The condition that q_{zz}, rather than q_z, vanish at $z=H$ is used in order to maintain a linear vertical variation of water vapor mixing ratio near the top boundary.

persist (as is evident from the stream function fields of Figs. 2 and 5 of Part I.).

Fig. 1 shows fields of perturbation streamfunction ψ' (defined as the difference between the present and the initial stream function) for the dry solution of the surface jet and midtropospheric jet cases at the time $t=t_m=10$ h when moisture is first added to the solutions. The most important difference between these two fields is seen to be the location of the intense clockwise eddy within the frontal system with the warm air mass to the right. In the surface jet case, this eddy occurs on the cold side of the surface front, whereas in the midtropospheric jet case it is located on the warm side of the front. As we shall see in the discussion which follows, these differences produce very different results in the evolution of the moist convection when water vapor is added to the solution.

In the solutions presented in this and the next section, moisture will be added to the dry solution suddenly at time t_m (10 h here) by prescribing a relative humidity field which is uniform in x. Because horizontal temperature variation is confined primarily to the frontal zone at this time, the resulting initial moisture field will consist of a horizontally uniform field of moist air in the warm sector ahead of the front. This rather unrealistic procedure was employed here because of its simplicity and will be modified in Section 5 in an effort to simulate a more realistic situation.

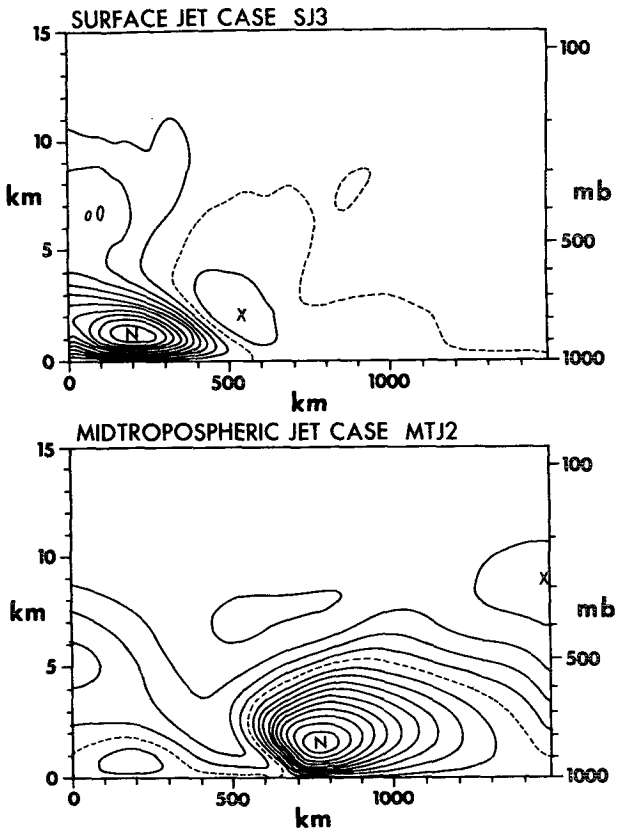

FIG. 1. Perturbation streamfunction fields for the surface jet and midtropospheric jet configurations at time $t=t_m=10$ h when moisture is added to the dry solutions. The contour interval $\Delta\psi'$ is 250 kg (m s)$^{-1}$. The maximum and minimum ψ' values, denoted respectively by X (counterclockwise circulation) and by N (clockwise circulation) are: 470 and -2750 kg (m s)$^{-1}$ in the surface jet case; 1090 and -2690 kg (m s)$^{-1}$ in the midtropospheric jet case.

a. Surface jet configuration

The surface jet configuration is characterized by a strong negative y-velocity at the surface which produces a strong clockwise circulation to the left of the front and a much weaker counterclockwise circulation in the warm air above and to the right of the front at the time $t=10$ h, as shown in the upper frame of Fig. 1. Thus when moisture is added, condensation should first occur at the point of maximum lifting in the clockwise cell on the cold side of the surface front. Condensation within the counterclockwise cell will require considerably more time because the maximum upward velocity is only $\frac{1}{3}$ of the value in the clockwise cell.

Fig. 2 shows the evolution of the cloud formation within the frontal system for the surface jet case. Over the time period shown, the surface front moves to the right with an average speed $U_f=3.7$ m s^{-1}. The dashed lines shown in Fig. 2 denote lines of constant streamfunction ψ_f' relative to a frame of reference moving to the right at a speed $U_f=3.7$ m s^{-1}, i.e., streamfunction ψ_f' is defined as

$$\psi_f' \equiv \int_0^z \rho_0(u-U_f)dz.$$

The first cloud formation is apparent in the figure at $t=17.43$ h in the cold region some 600 km upwind of the surface front which is in the region of upward motion of the clockwise cell shown in Fig. 1. Condensation first occurs at this point at $t=15.9$ h, some 6 h after moisture was added to the model. As indicated by successive frames in the figure, this cloud is convectively stable because temperatures below 1000 m upwind of the front are 10°–12° colder than they are downwind of the surface front.

Condensation first occurs in the warm air at 17.6 h at a point above the nose of the front. The sequence of frames in Fig. 2 after 19 hours shows this cloud to become unstable with the moist convection deepening with time. The front-cloud system moves more rapidly than the surface air ahead of the front; therefore warm, moist air is drawn up into the cloud as the frontal system overtakes it. As this unstable air rises into the convective zone, it encounters the more rapidly moving air above the front and is carried downwind ahead of the front ($t=19.43$ and 21.87 h of Fig. 2). The cloud deepens, and the wind speed, which increases with height, causes an "anvil" to form in the upper part of the cloud. The center of the zone of condensed cloud

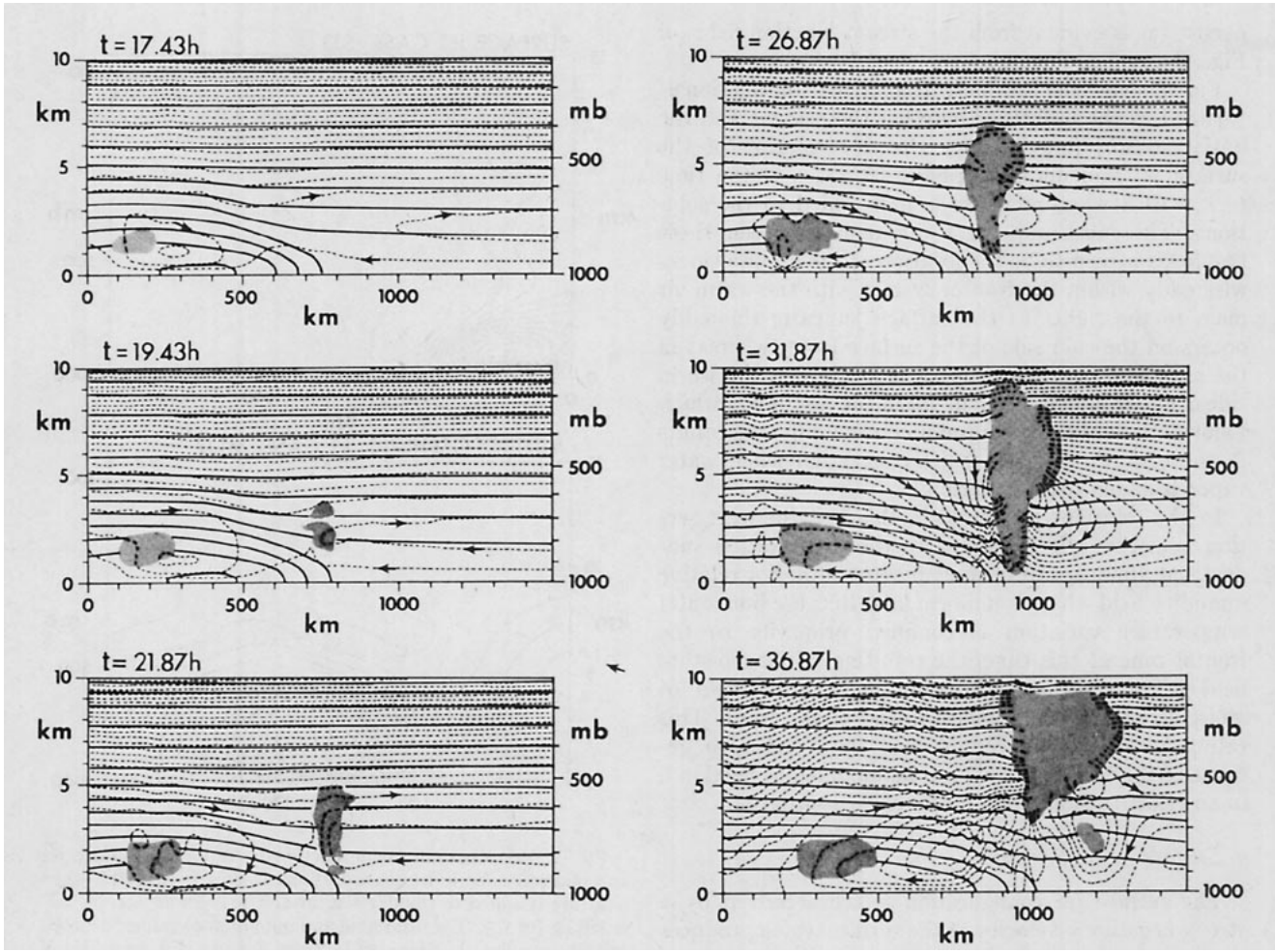

FIG. 2. Time sequence of composite contour plots for the moist surface jet configuration. Solid lines show potential temperature θ contours with $\Delta\theta = 4°C$. Dashed lines denote streamfunction contours [$\Delta\psi = 400$ kg (m s)$^{-1}$] for winds relative to an observer moving with the average frontal speed $U_f = 3.7$ m s^{-1}. Arrows on the dashed lines show wind direction. Shading denotes the presence of condensed water c. Only the lower 10 km of the model domain are shown in each frame.

water then begins to move off the nose of the front. Note also in the frame at 26.87 h that drier air at a height of 5000 m is being drawn down to the cloud base from the left of the cloud.

The maximum updraft intensity occurs within the convective cloud at around 32 h as shown by the plot of w_{max} versus time in Fig. 3. The plot shows a maximum vertical velocity within the cloud of approximately 1 m s^{-1} which must be viewed as an average value over the horizontal grid size of 20 km. At this point, the frame $t = 31.87$ h in Fig. 2 shows the convection-induced circulation to completely dominate the weaker circulation associated with the front. Also the intense cloud circulation disrupts the isentropes within the frontal system near the surface. Note that the cloud top is approaching the level of the tropopause at 10 km.

As Fig. 3 shows, the maximum vertical velocity w_{max} decreases rapidly after 32.5 h, reaching a more constant level of .15–.20 m s^{-1} after 36 h. The frame $t = 36.87$ h in Fig. 2 shows a breakdown in the streamfunction contours into a field of gravity waves which propagate away from the original convective system. The organized updraft near the base of the cloud is gone at 36.87 h, and further penetration of the cloud has been prevented by the tropopause. Thus the cloud tends to dry out from below while the top of the cloud flattens just below the tropopause.

The breakdown of the convective system and the apparent deterioration of the numerical solution may be attributed to several possible causes. First of all, the coarse spatial resolution of the convective region prevents the model from adequately representing the cloud structure to the extent which may be necessary in order to maintain the cloud system. Second, the two-dimensionality of the numerical model does not permit air to flow horizontally around the convective zone, thereby producing unrealistic winds as the cloud becomes a barrier to the mean flow. These winds may interfere with the updraft of warm moist air within the cloud and thereby could halt further cloud development. Finally, the absence of rain water phase as a

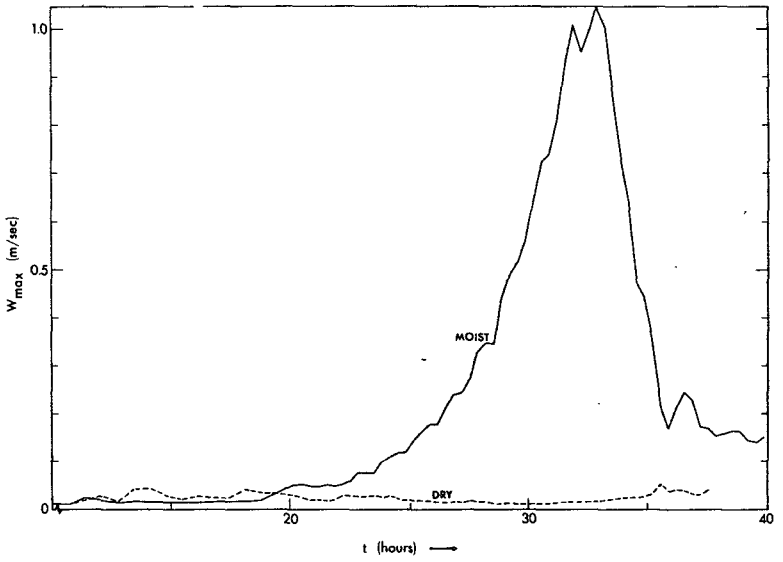

FIG. 3. Time history of the maximum vertical velocity w in the dry and moist solutions of the surface jet case.

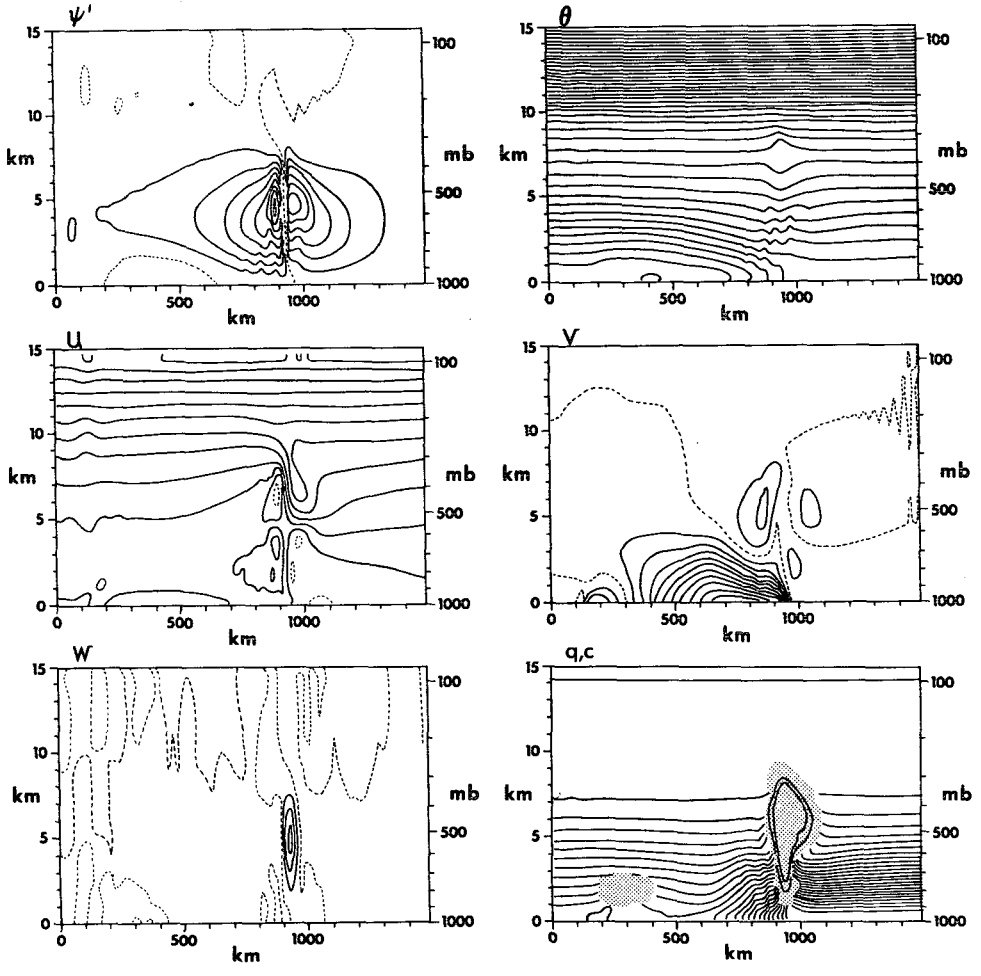

FIG. 4. Contour plots of variables from the moist surface jet solution at time $t=31.87$ h, the approximate time of maximum convective intensity. Contour intervals are $\Delta\psi'=2000$ kg (m s)$^{-1}$, $\Delta\theta=3$°C; $\Delta u=3$ m s^{-1}, $\Delta v=3$ m s^{-1}; $\Delta w=0.25$ m s^{-1}, $\Delta q=0.5$ g kg^{-1}; $\Delta c=0.5$ g kg^{-1} (for contours within the shaded region).

constituent within the model prevents the formation of a "cold air dome" such as is often observed beneath a large rain cloud as a result of evaporative cooling of falling rain water. Such a cold air dome is believed to be a mechanism for maintaining the updraft of warm moist air in a moving convective cloud system (Newton, 1950).

The distribution of different flow variables around the time of maximum vertical velocity within the cloud is shown in Fig. 4. The field of perturbation streamfunction indicates that the large upward velocity within a 40 km wide zone in the convective cloud is compensated by a weak downward motion in a region

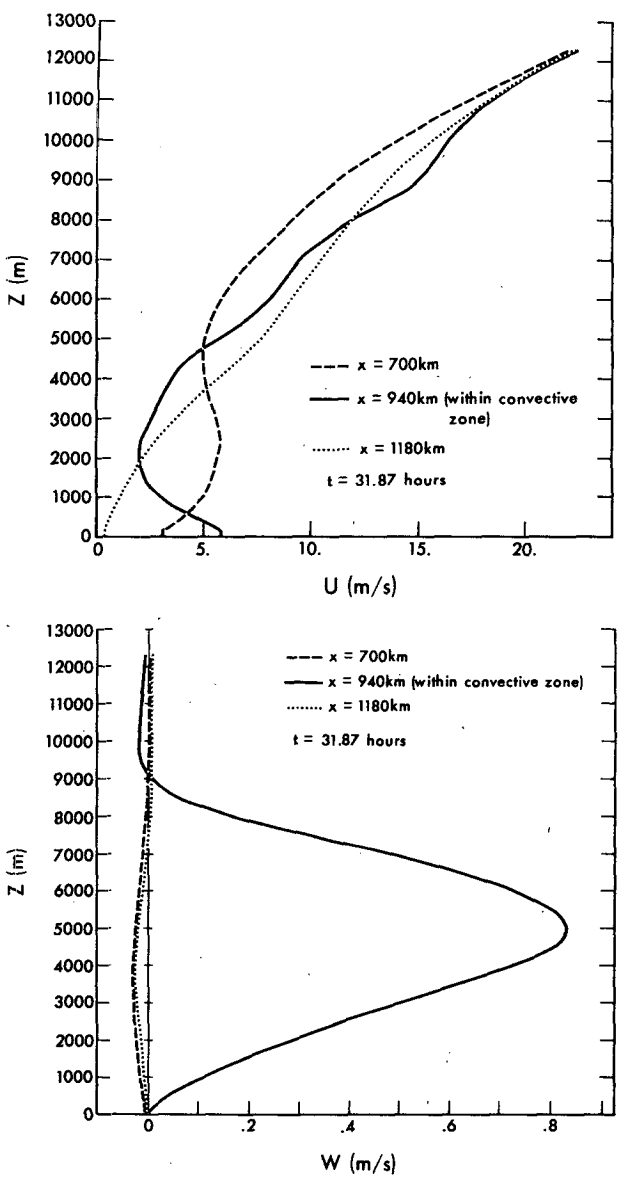

FIG. 5. Vertical profiles of the velocity components u and w at time $t=31.87$ h in the surface jet solution for stations upwind of, within, and downwind of the convective zone.

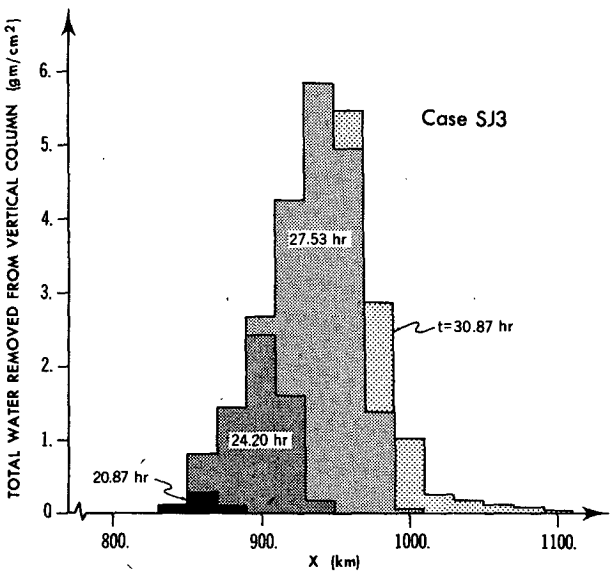

FIG. 6. The variation in time of the horizontal distribution of total water removed from each vertical column in the surface jet solution by the "rain" mechanism described in the text.

extending some 400 km to each side of the cloud. In the map of the x-velocity component u, the local maxima and minima of u near the top and bottom of the convective zone indicate the regions of strong convergence and divergence. Also, the weak blocking effect of the cloud at this time is indicated by the reduction of the x-velocity extending 800 km upstream to the left of the cloud at the 4000 m level and by the negative streamfunction zone extending upstream over this same region. The potential temperature and y-velocity contour maps show the disruption of the frontal system by the strong convection and the condensation heating within the cloud. Finally, the contours of mixing ratios of vapor and condensed water phases indicate the large difference in water vapor content of the air to the right and left of the surface front region.

More detailed indicators of the wind distribution in the vicinity of the convective zone are given by the vertical profiles of u and w in Fig. 5 at time $t=31.87$ h for horizontal stations within and to either side of the cloud. The w profiles show the strong updraft within the cloud with a maximum of 0.8 m s^{-1} at 5000 m and a weak downward velocity on both sides of the cloud with velocities of 3 cm s^{-1} or less. The u profiles indicate differences of as much as 4 m s^{-1} in the horizontal wind u on either side of the convective zone, primarily as a result of the convection-induced circulation.

Although the mechanism for generating rain water in the model is quite crude, it is still of interest to relate the rate at which water is removed from the model as "rain" to the evolution of the convective system as given by Figs. 2 and 3. As stated in Section 2, when the condensed water mixing ratio exceeds the threshold

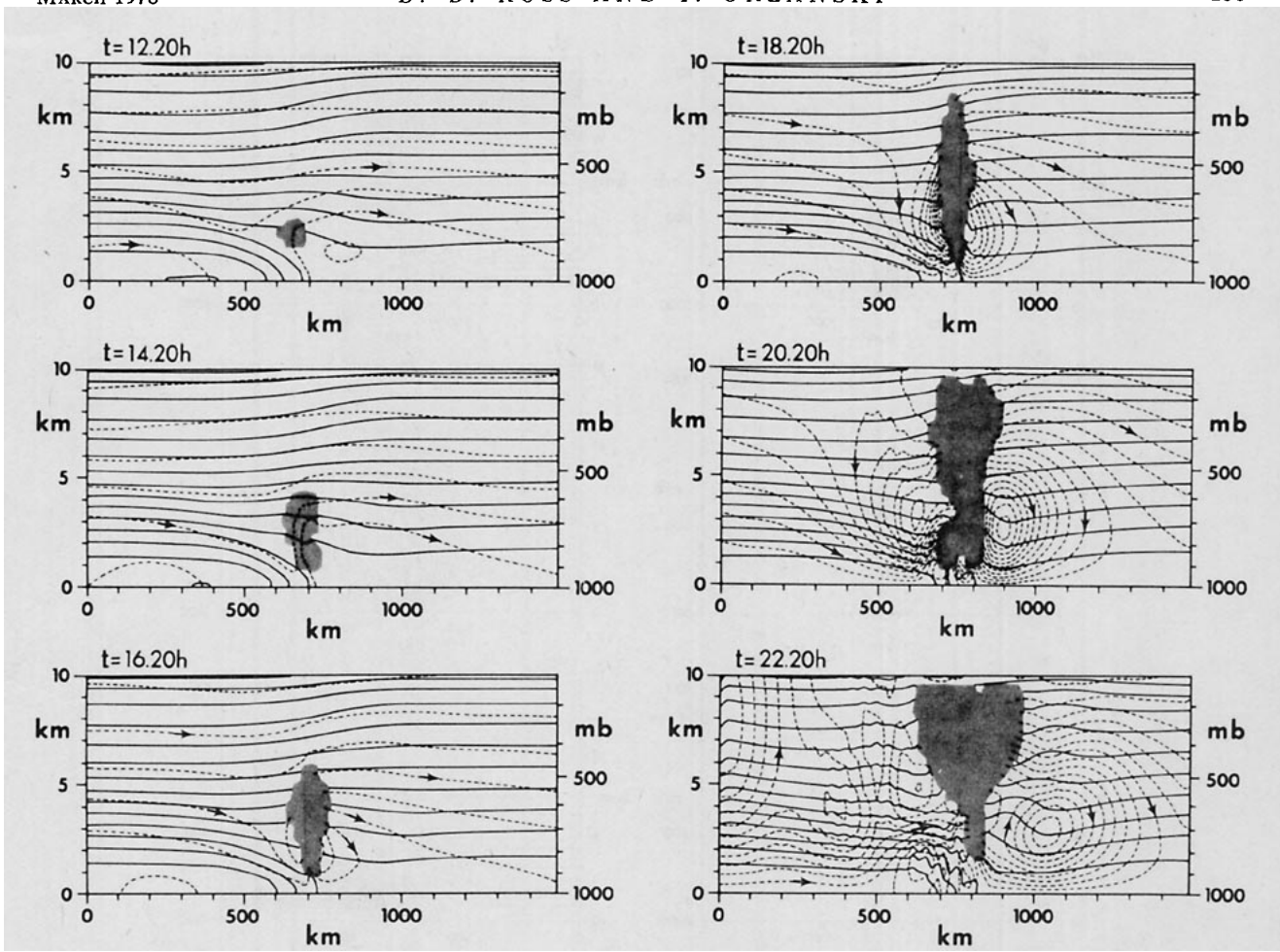

FIG. 7. Time sequence of composite contour plots for the moist midtropospheric jet solution showing potential temperature (solid lines), streamfunction (dashed lines) for an observer moving with the average frontal speed $U_f = 2.5$ m s^{-1}, and condensed water (shaded region). Contour intervals are identical to those in Fig. 2.

value of 1.5 g kg^{-1} at any point, the excess water phase at that point is removed from the model to simulate an irreversible rain-generation process. The total water removed from each vertical column would then represent the rain which would fall to the ground at that point if evaporation and horizontal advection were neglected. Fig. 6 shows the variation of this quantity as a function of time and x location in the present case SJ3. As one might expect, the location of the maximum rainfall rate corresponds to the location of the maximum upward vertical velocity. Reference to Fig. 3 shows that, after an initial delay which is necessary to permit the condensed water in the cloud updraft to achieve the rain threshold, the rate of water removal in Fig. 6 grows with the increase in w_{max}. However the rainfall rate peaks before w_{max} at 27.5 h (as the w_{max} location moves higher into the drier upper air) and then decreases to zero at around 35 h when w_{max} has leveled off at 15–20 cm s^{-1}. The "rain" occurs in a zone at the nose of the front as the front moves to the right; this zone is initially 3 grid points or 60 km wide but later broadens as the updraft region spreads and weakens.

b. Midtropospheric jet configuration

As was pointed out in Part I, the midtropospheric jet configuration is more representative of realistic frontal systems, since its maximum jet intensity occurs in the middle troposphere, well above the planetary boundary layer. In the streamfunction comparison of Fig. 1, it is evident that the intensity of the dry cross-stream circulation in the potentially unstable warm air of the MTJ2 case is considerable greater than it is in the SJ3 case. In particular, the vertical velocity in the warm zone above the front in the case MTJ2 is as much as 2.2 cm s^{-1}, whereas upward motion in the warm zone of the case SJ3 is only 0.2 cm s^{-1}. Hence one would expect condensation to occur at this point much more rapidly than was observed in the previous surface jet case.

The actual evolution of the moist case MTJ2 is shown in Fig. 7 which is analogous in format to Fig. 2 but with the frontal speed $U_f = 2.5$ m s^{-1}. The only condensation to occur in this case appears in the warm zone above the nose of the front. Condensation first

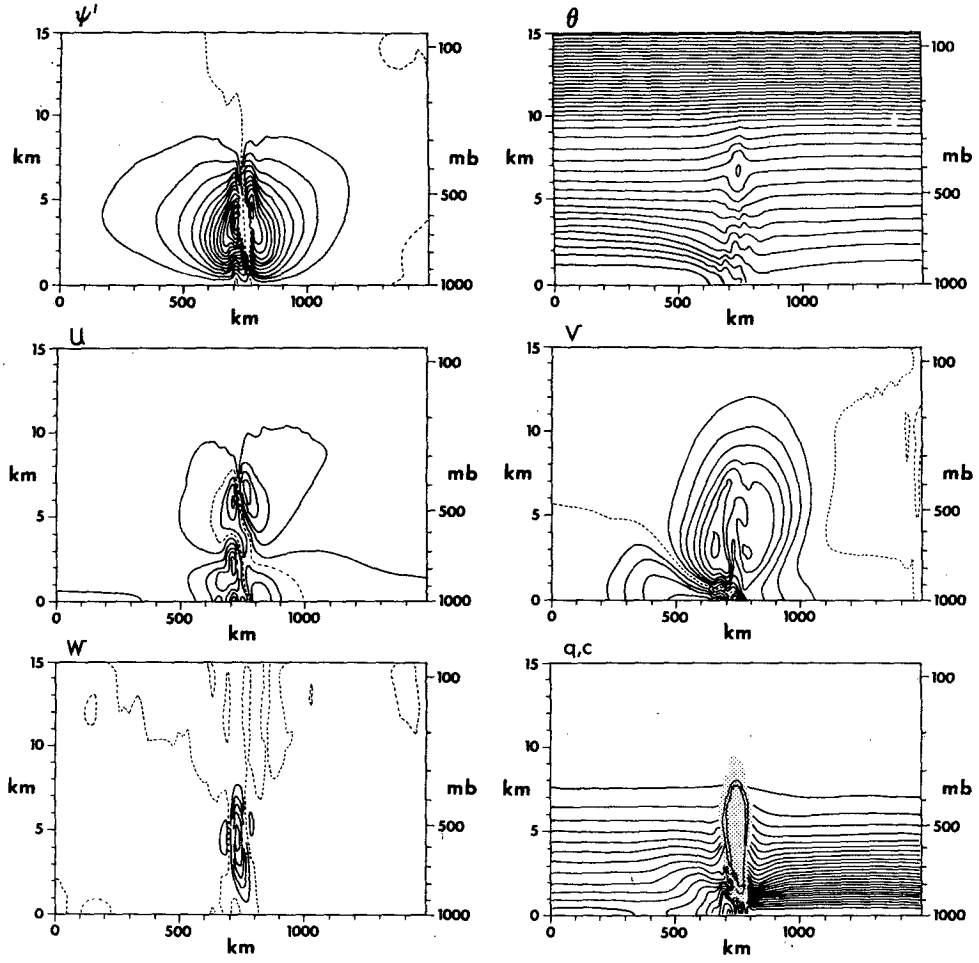

FIG. 8. Contour plots of variables from the midtropospheric jet solution at time $t=18.87$ h when convective activity is maximum. Contour intervals are: $\Delta\psi'=2000$ kg (m s)$^{-1}$, $\Delta\theta=3$°C, $\Delta u=3$ m s^{-1}, $\Delta v=4$ m s^{-1}, $\Delta w=0.25$ m s^{-1}, $\Delta q=0.5$ g kg^{-1}, and $\Delta c=0.5$ g kg^{-1} (for contours within the shaded region).

occurs at this point at 11.7 h, showing a 1.7 h delay after moisture was added to the model. (This compares with the 7.6 h delay before condensed water appeared in the warm air in case SJ3.)

The development of the convectively unstable cloud is similar to that found in the surface jet case except that the cloud growth is considerably faster in the present case, due to the larger initial vertical velocity. Maximum intensity in the updraft of the cloud system is 1.8 m s^{-1}, which occurs at 18.9 h or 7.2 h after condensation first occurs. A direct comparison between cloud development in the present MTJ2 case and the SJ3 case of the previous subsection is not proper since the nonlinear eddy viscosity coefficient C was reduced from 1.0 in the previous case to 0.75 in the present case. In order to permit this comparison, another surface jet solution was obtained which is identical to the previous case except that C was set equal to 0.75 in order to match the current model conditions. The resulting vertical velocity maximum in this revised solution is 1.2 m s^{-1}, which occurs at 31.2 h or 13.6 h after condensation first was detected in the warm air.

The convective system in the midtropospheric jet case grows to peak intensity in approximately half the time that was required by the surface jet case (7.2 versus 13.6 h). For an actual atmospheric frontal system, environmental conditions will change due to diurnal effects (and, to a lesser extent, due to synoptic changes); also, orographic effects may alter surface boundary conditions as the frontal system moves. Therefore, this difference by a factor of 2 in the development times of the two convective systems indicates that there is considerably less likelihood of the surface jet system producing a fully developed storm system when compared with the midtropospheric jet case.

The vertical velocity in the updraft decreases quite rapidly after reaching its peak at 18.9 h. As frames $t=20.20$ and 22.20 h of Fig. 7 show, the decrease in the updraft intensity in the cloud produces gravity waves which radiate away from the cloud in a similar manner

to that found in the SJ3 case in Fig. 2. A discussion of the development of this gravity wave field will be given in the next subsection.

As the convective cloud reaches the tropopause and halts its penetration, the cloud spreads symmetrically about the original updraft zone. Because the wind shear is weak in this case compared to the SJ3 case, no asymmetric cloud formation (or "anvil cloud") develops. Also because of the weak wind shear, the center of the convective system remains over the nose of the front throughout the duration of the numerical solution.

Contour maps of various different quantities from the case MTJ2 are shown in Fig. 8 for the time $t=18.9$ h, the time of maximum vertical velocity in the cloud updraft. The circulation produced by the convective system is very similar to that shown in Fig. 4 for the surface jet case except that the blocking effect of the cloud, as indicated by the broader extent of the perturbation streamfunction field ψ' upwind of the cloud, is weaker in the present case due to the weaker wind shear. Also, because the vertical velocity is stronger in the MTJ2 case, the condensation heating in the cloud produces a larger disturbance of the potential temperature field in this case than in the SJ3 case. It is this disturbance of the isentropes, together with the advection field shown by the maps of ψ', which will generate gravity waves as the updraft intensity within the cloud decreases after reaching its peak value.

c. *Gravity wave generation*

As was noted, gravity waves are generated in the two numerical solutions described above as the moist convection achieves its maximum intensity and begins to weaken. A strong and well-organized gravity wave response is particularly evident in the midtropospheric jet solution MTJ2 shown in Fig. 7 in the region downwind of the cloud-front system at 20.20 and 22.20 h. The propagating gravity wave is indicated in the frame at 22.20 h by the closed circulation, a remnant of the cloud circulation, with a streamfunction minimum located at 1050 km in x and at a height of 3000 m. Accompanying this circulation, the field of potential temperature contours shows a trough line and a crest line (i.e., the loci of points along the contours where the contour height is minimum and maximum respectively) extending from near the base of the cloud upward and to the right. The trough line denotes the position of the gravity wave front which appears to have been generated in the lower part of the cloud and which is propagating away from the cloud to the right.

Fig. 9 shows the successive positions of the wave crest and trough at two-hour intervals as the gravity wave propagates to the right. The indicated cloud positions at the initial and final times for the figure show that the gravity wave crest and trough tend to move considerably faster than the cloud with the exception of the lower part of the crest line. The inclusion

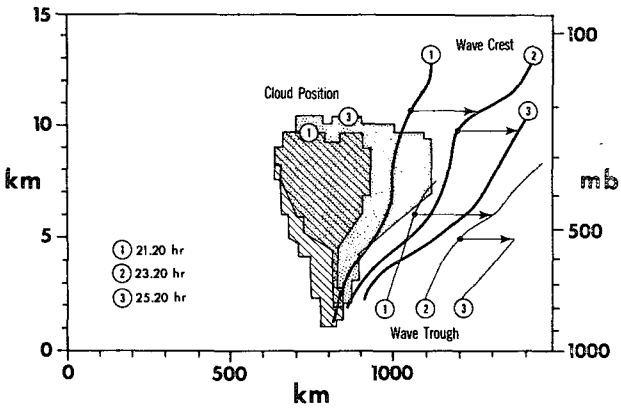

FIG. 9. Schematic figure showing locations of the gravity wave crest and trough in the midtropospheric jet solution at three different times. Two positions of the condensed water zones are also included for comparison.

of the upper 5000 m of the model domain in Fig. 9 (the frames in Fig. 7 excluded the solution above the tropopause at 10 000 m) shows the effect of the three-fold increase in the stratification above 10 000 m in steepening the slope of the wave crest.

While Fig. 9 shows a well-defined gravity wave which can be expected to propagate for a considerable distance downwind of the cloud-front system, it is not possible to determine the long time character of the propagating wave in the present case because of the limited domain of the numerical solution. The development of the wave as indicated by the crest and trough lines shows a great deal of variation in the horizontal wave length and phase speed. In particular, the slow propagation speed of the wave crest below 5000 m causes the apparent wavelength at this level to increase drastically with time. However, typical horizontal wavelengths and phase speeds between 5000 and 10 000 m are 300 km and 20 m s^{-1} respectively.

These values are similar to the characteristic features of gravity wave phenomena observed in the vicinity of frontal zones in satellite cloud photographs by Dr. A. Gruber (private communications). In fact, the gravity wave produced in the numerical solution is also suggestive of the gravity wave phenomena reported in a number of different mesoscale observational studies (e.g., Brunk, 1949; Bosart and Cussens, 1973; Uccellini, 1975). Investigators (e.g., Brunk, 1949; Bosart and Cussens, 1973) frequently have associated the origins of these waves with zones of strong convective activity. The waves observed in such studies have been found to propagate over distances of 1000 km or more and to have durations of as long as 15 h. These observations indicate that the lifting associated with intense gravity waves may trigger new convection in regions which are potentially moist unstable. Hence it is possible that strong convection similar to that modeled here could cause new storms to occur at large distances from the

TABLE 1. Characteristic values for initial relative humidity profiles.

z (km)	RH(70%max)	RH(80%max)	RH(90%max)	RH(90%/50%)
0	62%	71%	80%	80%
2	70%	80%	90%	90%
3	—	—	—	50%
10	—	—	—	5%
15	31%	35%	40%	5%

initial storm through the triggering mechanism of propagating gravity waves.

4. Solution sensitivity to initial humidity and temperature

The location and intensity of latent heat release is determined not only by the dry frontal circulation but also by the humidity and temperature fields which are prescribed as initial conditions. In Section 5, attention will be given to the case in which relative humidity varies in x ahead of the front so that the cold front may overtake a surface layer of moist air to initiate unstable convection. In the present case, we will investigate the sensitivity of the moist frontal system to different initial vertical profiles of humidity when the initial relative humidity fields are uniform in x. Also a comparison will be made between solutions with the same initial relative humidity field but with initial temperature fields differing by 10°C to show seasonal differences in the stability of the moist atmosphere.

a. The initial moisture field

The initial vertical profile of relative humidity determines the onset time of condensation (if such condensation is to occur) as well as the subsequent development of the convection. In fact the time required for condensation to occur and for a state of free convection to be achieved would be crucial in an actual atmospheric situation, since orographic, diurnal, and synoptic conditions might prevent the storm from ever developing if this time delay is too long.

To demonstrate the humidity dependence of the present numerical solutions, four cases having different humidity profiles will be compared. All four cases start with the same initial temperature and wind fields as the solution of MTJ2 described in a previous subsection. Then, as has been the procedure before, the appropriate moisture field will be added to each solution at time $t=10$ h with the different piece-wise linear relative humidity profiles for the four different cases as shown in Table I. The first three cases, denoted as RH(70% max), RH(80% max), and RH(90% max), have similar functional distributions but with different factors so that the relative humidity maximum at 2000 meters ranges from 70% to 90%. (Note that the RH(90% max) case is the original solution for MTJ2 discussed earlier.) The fourth case, denoted as RH(90%/50%), is the same as RH(90% max) below 2000 m but contains a rapid decrease in moisture to 50% relative humidity from 2000 to 3000 m to simulate the frequent occurrence of dry air above a moist surface layer as is often observed in atmospheric soundings taken in the southern Plains States of the United States.

Ideal parcel theory provides useful indicators of the potential for instability in the warm air zone. Table 2 shows the values of several quantities indicative of parcel instability as determined for the present four cases at the initial time $t=10$ h and at different levels in the warm air mass far downstream of the front. (Virtual temperature effects are not included in the parcel theory results shown in Table 2.) The quantity Δz_{cond} is the distance a parcel must be lifted adiabatically from the initial height z_0 in order to achieve saturation (95% for saturation). The quantity Δz_{FC} is the total distance the parcel must be lifted, adiabatically when unsaturated and pseudoadiabatically thereafter, from its initial level in order to achieve a state of free convection (i.e., a state in which the lifted saturated parcel has attained a temperature equal to the environmental temperature at that level due to condensation heating and will be buoyantly unstable if further lifting occurs). The third quantity is the distribution of equivalent potential temperature θ_e in the lower 3000 m, which is an indicator of the potential for convective instability. In addition, the θ_e distribution indicates the intensity of the eddy viscosity if the region is saturated since the eddy viscosity in saturated air is assumed to depend upon the equivalent potential temperature gradient θ_{e_z} when this quantity is negative (Eq. (2.13)). Finally the stability index SI is Showalter's (1953) index, which is a measure of the potential buoyancy of an atmospheric column. The index is defined to be the difference between the ambient temperature at

TABLE 2. Stability indicators at height z_0 for different initial humidity profiles.

	Δz_{cond}(m)				Δz_{FC}(m)				θ_e(K)				
z_0(m)	0	1000	2000	3000	0	1000	2000	2500	0	1000	2000	3000	Stability index (K)
RH(70% max)	1070	820	600	700	1410	2000	∞	∞	336	327	322	318	0.0
RH(80% max)	900	610	410	590	1150	1330	1950	∞	339	329	325	321	−1.5
RH(90% max)	570	380	220	280	740	610	800	1390	346	333	326	323	−2.5
RH(90%/50%)	570	380	220	1100	740	610	800	∞	346	333	326	316	−2.5

TABLE 3. Cloud development times and convection parameters for different initial humidity profiles.

	RH(70% max)	RH(80% max)	RH(90% max)	RH(90%/50%)
Δt_{cond} (h)	10.3	5.6	1.6	1.9
Δt_{FC} (h)	14.5	7.9	3.9	4.5
$\Delta t_{w_{max}}$ (h)	23.5	13.5	8.9	10.9
w_{max} (m s^{-1})	0.70	1.04	1.78	1.69
z_{max} (cloud) (m)	7800	8500	9500	9200

500 mb and the temperature of a parcel lifted (adiabatically to saturation and pseudoadiabatically thereafter) from 850 mb to 500 mb.

Table 2 shows clearly the expected increase in potential instability of the warm air mass as the relative humidity of the surface layer is increased. In particular, the increase in the 2000 m humidity peak from 70% to 90% causes nearly a threefold reduction in the height Δz_{cond}. Similarly as the moisture content increases, the displacement Δz_{FC} required for free convection decreases for a fixed initial height while the maximum initial height of a parcel which can achieve free convection (i.e., Δz_{FC} finite) increases. Finally, the stability index is seen to decrease from 0 to -2.5°C where, according to Showalter (1953), values from $+1$ to -2°C are found to indicate some probability that thunderstorms will occur while values of -3°C or lower indicate a potential for severe thunderstorms. The case RH(90%/50%) shows the effect of the lower humidity above 2000 m by the large value of Δz_{cond} at 3000 m and the infinite Δz_{FC} at 2500 m. In addition, the 10°C drop in θ_e between 2000 and 3000 m indicates the large potential for convective instability across this layer as well as the possible occurrence of larger eddy viscosity values in the numerical model if the region becomes saturated.

The quantities given in Table 3 indicate the actual development of the cloud zone in the numerical solutions for the four humidity cases. The time Δt_{cond} is the time elapsed after the moisture field is added to the dry solution (at $t=10$ h) until a condensed water phase first appears in the solution. The time Δt_{FC} is the time elapsed after moisture is added until the time when free convection is first detected; specifically we will define this to be the time when the upward velocity in the moist solution is first observed to be twice the maximum upward velocity observed in the dry solution. (This latter value was 3.3 cm s^{-1} for the dry solution MTJ2.) The time $\Delta t_{w_{max}}$ is the time elapsed after moisture is added until the maximum vertical velocity w_{max} is achieved. The maximum velocity w_{max} is an indicator of the intensity of convective activity in the cloud system. Finally z_{max} (cloud) is the maximum height of the cloud top at the time when the intense upward motion in the cloud has ceased.

In all four cases, saturation first occurs around the 2000 m level since Δz_{cond} is a minimum for $z_0=2000$ m. However, the time Δt_{cond} required to reach condensation is not proportional to Δz_{cond} but rather is considerably longer for the lower humidity profiles than one would expect if constant adiabatic lifting occurred. This might be due, in part, to diffusion of water vapor and temperature but is more likely the result of spatial and temporal variations of the vertical motion field. As indicated by the contours of perturbation streamfunction in case MTJ2 of Fig. 1, the region of strong upward motion extends from 500 to 2500 m height in a sloping zone over the nose of the cold front with a width of approximately 100 km and a maximum of 3 cm s^{-1} at 2000 m. However, within this region the vertical velocity will vary considerably in space and time so that the larger vertical displacement of 600 m required for condensation in the case RH(70% max) will take much longer time than the 220 m displacement needed for cases RH(90% max) and RH(90%/50%).

The effective average lifting speed for the first air parcel to condense, assuming no diffusion effects, is the ratio $\Delta z_{cond}/\Delta t_{cond}$. Then using the smallest Δz_{cond}, namely that at $z_0=2000$ m, we obtain values of 1.5, 2.0, 3.7, and 3.2 cm s^{-1} for the cases RH(70% max), RH(80% max), RH(90% max) and RH(90%/50%), respectively. Since typical maximum vertical velocities of 3 cm s^{-1} are observed in the dry solution in the lifting zone, these values seem to be quite reasonable and demonstrate the reduced average vertical velocity which is encountered by the parcels in the lower humidity cases over the longer displacement distances required.

One may derive a similar average lifting speed by calculating $(\Delta z_{FC}-\Delta z_{cond})/(\Delta t_{FC}-\Delta t_{cond})$ for the time between first condensation and free convection. Since saturation first occurs at around 2000 m in all four

cases, one may assume that the saturated parcels originated at a height below 2000 m. Taking values of Δz_{FC} and Δz_{cond} from these heights, one then finds estimated average lifting speeds over this period to range from 6 to 10 cm s^{-1} whereas the observed maximum vertical velocities during this period vary from 3 cm s^{-1} when condensation first occurs to 6 cm s^{-1} as the parcel achieves the prescribed condition for "free convection" (i.e., a doubling of the maximum vertical velocity from the dry solution).

The above analysis demonstrates that, although dynamic lifting of moist air parcels by the frontal circulation provides an acceptable explanation of the time differences required to achieve initial condensation, this same dynamic lifting is not sufficiently intense to explain the subsequent time required to achieve free convection. The additional mechanism acting in the model to accelerate this process is the eddy viscosity which is activated in the regions of convective instability ($\partial\theta_e/\partial z<0$) in the lower part of the model (below 4000 to 5000 m, depending upon the humidity profile). These diffusive effects in the model may be as important as the dynamic lifting of air parcels once saturation has occurred.

The dependence of the eddy viscosity upon unstable vertical gradients of equivalent potential temperature is included in the model in order to simulate the expected strong subgrid-scale turbulence which would occur. This viscosity in the model appears to accelerate the upward transport of saturated air parcels through vertical diffusion. On the other hand, in saturated air when such moist unstable conditions are present, horizontal diffusion may slow the onset of instability of saturated parcels resolved by the model through the entrainment of drier ambient air from outside of the cloud. The longer time Δt_{FC} shown in Table 3 for the case RH(90%/50%) compared to RH(90% max) shows the slight stabilizing effect of such entrainment because the air outside of the saturated zone is considerably drier in the former case.

The smaller values of w_{max} and the larger values of $\Delta t_{w_{max}}$ for cases RH(70% max) and RH(80% max) (compared to the two cases with 90% maximum humidity) result from the initially weaker convective instability of those two cases (Table 2) and the effect of this upon the updraft intensification. Another indication of this is the smaller Stability Indices of these cases as shown in Table 2. Note also that the maximum vertical velocity w_{max} of the case RH(90%/50%) with a drier upper troposphere is only 5% smaller than that of case RH(90% max), thus showing that the moisture content of the lower atmosphere is the predominant factor determining the intensity of the convection as one might expect. However, it may also be argued that the greater virtual temperature contrast between the cloud and surrounding air in case RH(90%/50%) counteracts the stabilizing effect of dry air entrainment.

The very coarse horizontal resolution which permits only one "cloud" and one "updraft" to occur in the convective zone forces the maximum vertical velocity in the updraft to be more than an order of magnitude smaller than would occur in an actual cloud updraft. As a result, the time ($\Delta t_{w_{max}}-\Delta t_{FC}$) for a mature convective system to develop after free convection occurs is considerably longer than would be required for an actual severe storm. Also the broad updraft with low vertical velocity (compared to the narrow, very intense updrafts observed in actual severe storm clouds) does not permit penetrative convection into the stratosphere (above 10 000 m) such as might be expected for unstable atmospheric conditions in cases RH(90% max) and RH(90%/50%). Rather the cloud tops in the numerical solutions only reach the upper troposphere as shown by the values of z_{max} (cloud) in Table 3.

b. The initial temperature field

The exponential dependence of saturation vapor pressure upon temperature causes the value of temperature to be very important in determining whether a saturated region will become convectively unstable. This effect can be seen in the case SJ3 shown in Fig. 2. The strong vertical lifting produced by the frontal circulation causes the air to saturate between 1000 and 2000 m within the cold air mass 500 km upwind (to the left) of the surface front. However, because the air at this height is 10° colder than air at the same height in the warm region, the saturated air is convectively stable and thus forms a stable cloud which always remains below 2500 m. On the other hand, as described earlier, when lifting causes saturation in the warm air at $z=2000$ m above the nose of the front, this saturated air becomes unstable and produces moist convection which almost reaches the tropopause.

This thermodynamic effect of temperature upon cloud development can also be demonstrated by reducing the overall temperature of the solution by a constant amount. To do this we have produced a solution which is identical to the surface jet case shown in Fig. 2 except that the reference temperature Θ_0 for the surface temperature in the warm air mass far downwind of the front is reduced from 24°C to 14°C. A comparison of this new solution to the solution shown in Fig. 2 would be similar to a comparison of a late spring and a late winter situation in the midwestern United States. The 10° reduction in potential temperature over the entire field has virtually no effect upon the dry frontal circulation as indicated by the nearly identical circulations which resulted from the two solutions at $t=t_m=10$ h when moisture was added. However, the effect of the temperature reduction in the moist case is to cause the region of potential convective instability ($\partial\theta_e/\partial z<0$) in the warm air mass to be reduced from the lower 5000 m in the case with $\Theta_0=24$°C (similar to the case RH(90% max) of the previous subsection) to

only the lower 2500 m for the case with $\Theta_0=14°C$. Fig. 10 shows the fields of water vapor and condensed water mixing ratios for the case with $\Theta_0=14°C$ at $t=31.9$ h, the same time as that of the fields shown in Fig. 4 (the case with $\Theta_0=24°C$). A comparison of the condensed water fields shows that the lower temperature produces a cloud which is only weakly unstable with an equilibrium level (the point where cloud parcels are neutrally buoyant) around 3500 m height. Condensed water mixing ratios in excess of 0.5 g kg^{-1} (marked by contours within the shaded region) are localized to a region between 2000 and 4000 m height with the wind as well as horizontal diffusion producing a cloud layer at the equilibrium level downwind of the main cloud. The vertical velocity within the cloud is 4.5 cm s^{-1} at this time and never exceeds 7 cm s^{-1} during the time span of the solution.

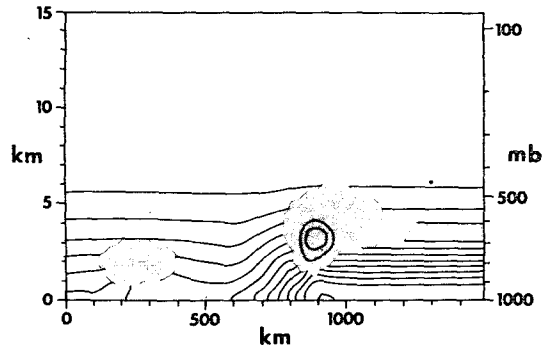

FIG. 10. Contour plot of mixing ratios of water vapor (contours outside of shaded region) and condensed water (contours within shaded region) at time $t=31.87$ h for the surface jet solution with the reference temperature Θ_0 reduced from 24°C to 14°C. Contour intervals are 0.5 g kg^{-1} for both mixing ratios.

5. Temperature inversion effects

The vertical temperature distribution can affect the dynamics of the frontal circulation through variations in the thermal stratification of the atmosphere. The most drastic manifestation of this is in the form of temperature inversions (highly stratified layers in which temperature increases with height). The occurrence of such inversions above a moist surface layer is an important indicator of the potential of an atmospheric environment to produce severe storms (Fawbush and Miller, 1953). In fact, the common precursor of severe storm activity in the midwestern United States is the northward advection of a surface layer of moist air from the Gulf of Mexico beneath an inversion layer separating the moist surface air from an overlaying warm dry air mass coming from the higher elevations to the west. As Fulks (1951) has observed, the capping inversion which separates these two air masses prevents moderate vertical motion due to weak surface heating or other effects from releasing the potential atmospheric instability prematurely before large convective instability has developed. In the case of a severe storm, this large convective instability is released explosively when the capping inversion is weakened sufficiently or is destroyed. There are various different ways to destroy this stable layer, including cooling of the upper air by horizontal advection or heating of the surface layer by horizontal advection or solar heating, both of which then allow moderate vertical lifting to release the instability. However, Beebe and Bates (1955) have shown that vertical lifting alone can destroy the capping inversion and release the convective instability if vertical displacement of the air column is large enough. The stable layer is weakened or destroyed by upward motion because the lower humidity in the air above the inversion causes this air to remain unsaturated and therefore to cool more rapidly than the moist air below, which saturates and releases latent heat as it is lifted.

So far, we have been studying the frontal circulation in atmospheric situations without a capping inversion. It is of interest for us to determine under what circumstances this circulation can produce lifting of a sufficient intensity to destroy such an inversion and release the convective instability which would otherwise be controlled. First, it is important to determine what effects the inversion will have upon the dry frontal circulation. To do this, we have altered the initial potential temperature of the case MTJ2 by adding a 6° temperature jump between 2180 and 2420 m. Also, in order to prevent diffusive smoothing of the temperature jump under stable conditions, the background diffusivity κ_0 of the model was reduced from 5 to 1 m^2 s^{-1} while the viscosity constant C which determines the eddy viscosity when θ or θ_e is unstable was increased from 0.75 to 1.25 so as to achieve similar eddy viscosity values within the cloud to those found in the earlier cases.

The composite contour map of potential temperature θ and perturbation streamfunction ψ' in Fig. 11 shows the effect which the inversion has upon the dry frontal circulation. The circulation in this figure may be compared with the circulation shown in Fig. 1 for the mid-tropospheric jet case without an inversion at a similar time. (An exact comparison can be made with the analogous contour map at $t=10.87$ h in Fig. 5 of Part I.) Although the vertical scale of the clockwise cell is very similar in both cases, the inversion is seen to inhibit vertical motion with the most intense circulation occurring beneath the inversion. In particular, although the maximum vertical velocities in both cases are approximately 2.3 cm s^{-1}, the height of the maximum at this time was reduced from 1840 m in the case without the inversion to 1400 m in the solution with the inversion. Also, as Fig. 11 shows, the presence of the inversion diverts much of the upward flow to the right to form a local x-velocity maximum beneath the stable layer.

When moisture is added to the dry solution, the

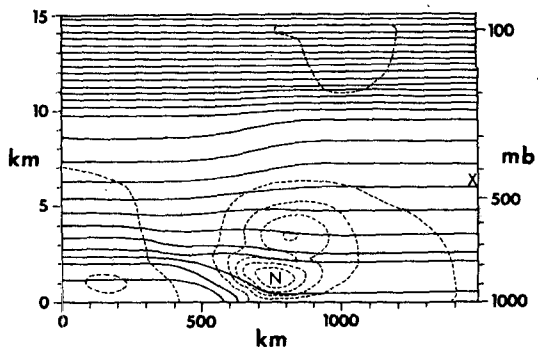

FIG. 11. Composite contour plot of potential temperature (solid contours) and perturbation streamfunction (dashed contours) for the dry midtropospheric jet configuration with a temperature jump $\Delta\theta_I = 6°C$ at the time $t = 10.88$ h. Contour intervals are: $\Delta\theta = 5°C$ and $\Delta\psi' = 500$ kg (m s)$^{-1}$. The maximum ψ' (denoted by X) is 440 kg (m s)$^{-1}$, and the minimum ψ' (clockwise circulation centered at N) is -2500 kg (m s)$^{-1}$. The location of the inversion is indicated by the two more closely spaced isentropes near 2.5 km height.

presence of the temperature inversion alters the development of moist convection considerably. First, the lowering of the vertical velocity maximum in the solution prior to condensation will reduce the height at which condensation initially occurs. Then as further lifting causes local free convection, the convective cloud penetrates the more stable inversion layer with a resulting reduction in convective intensity (shown by maximum vertical velocity) and a reduced maximum cloud height compared to the equivalent moist case without an inversion.

A set of calculations was performed to determine the effect upon various moist convection features when a potential temperature increase $\Delta\theta_I$ is added to all potential temperature grid values above 2180 m in the basic case MTJ2. This temperature increase produces a layer of increased stratification between the adjacent grid point rows at 2180 and 2420 m height. The solutions obtained also differ from the previous MTJ2 solution in that the background eddy diffusivity κ_0 is reduced to 1 m^2 s^{-1} so as to reduce the diffusion of the undisturbed temperature jump.

TABLE 4. Convection parameters and cloud development times for different temperature jump intensities.

	$\Delta\theta_I = 0°C$	$\Delta\theta_I = 3°C$	$\Delta\theta_I = 6°C$
w_{max} (m s^{-1})	2.04	1.32	0.45
$t(w_{max}) - t_M$ (h)	8.9	10.5	12.5
z (w_{max}) (m)	4730	4140	3310
z_{max} (cloud) (m)	11 000	8800	7100

Table 4 shows the dependence of cloud development upon the intensity $\Delta\theta_I$ of the temperature jump in these solutions. A comparison of the maximum vertical velocities (occurring within the cloud region) for the different cases indicates an approximate doubling of the w_{max} reduction as $\Delta\theta_I$ is doubled (a 35% reduction from $\Delta\theta_I = 0$ to 3°C and a 78% reduction from $\Delta\theta_I = 0$ to 6°C). Similarly the time increase required to achieve w_{max} is proportional to $\Delta\theta_I$; the proportionality to $\Delta\theta_I$ also applies to the reduction in the height z_{max} (cloud) of the cloud top. Thus, the present set of experiments indicates that the potential temperature jump in the model reduces the intensity and depth of moist convection in rough proportion to the magnitude $\Delta\theta_I$ of the temperature jump, as one might expect.

The cases discussed so far have been restricted to the development of moist convection along a two-dimensional front in a moisture field in which the air in the immediate vicinity of the front is near saturation from the beginning of the moist solution. In addition, the only possible triggering mechanism for deep convection in these solutions has been the lifting caused by the frontal circulation. In the real atmosphere, other competing mechanisms such as diurnal heating may act over a large area to release convective instability before the frontal system reaches the unstable air mass. On the other hand, as we have shown in the model, the presence of a capping inversion above the moist surface layer may be sufficiently strong to prevent surface heating alone from releasing the convective instability. Under such circumstances, the combined effect of surface heating and frontal lifting may be required to achieve deep convection. In the common springtime situation encountered in the midwestern United States, surface air at a given point becomes increasingly moist and therefore more unstable as a result of northward advection of a tongue of moist air from the Gulf of Mexico. This air is prevented from releasing its instability because of a strong capping inversion. Under such circumstances, the arrival of a front at this moist tongue may trigger violent severe storms due to the large convective instability which has developed.

The present two-dimensional model is unable to fully simulate the three-dimensional situation in which an eastward moving front encounters a developing tongue of moist surface air flowing northward. However, we are still able to demonstrate the competing effects of diurnal surface heating and frontal lifting in generating deep convection in a moist surface layer which is capped by an inversion, the magnitude of which may be varied. In this idealized case, the moving frontal system will initially be located in a drier air mass but will overtake the moist surface layer as the calculation progresses.

In the solutions to be presented, the following modifications of the initial conditions have been made to the case MTJ2:

1) The shear in the initial x-velocity wind U is

doubled by halving the scale height of wind variation so that

$$U(z)=2+3\tanh(z/2500).$$

2) A constant potential temperature increase $\Delta\theta_I$ is added to the grid point values θ of the original field at and above $z=1730$ m. This produces a strongly stratified layer between 1510 and 1730 m.

3) Because the inversion would be rapidly altered by the lifting associated with the frontal circulation, moisture is added to the dry solution at $t=t_M=5$ h instead of the original time of 10 h. Also, the relative humidity field R which is prescribed at this time contains x as well as z variation and is defined as

$$R(x,z)=R_1(z)+[R_2(z)-R_1(z)]\times 0.5[1+\tanh((x-x_0)/\delta)]$$

where $x_0=700$ km, $\delta=70$ km, and R_1 and R_2 are piecewise linear functions of z with the following reference values: $R_1=40\%$, $R_2=80\%$ at $z=0$ m; $R_1=50\%$, $R_2=90\%$ at $z=1510$ m; $R_1=R_2=40\%$ at $z=1730$ m; $R_1=R_2=30\%$ at $Z=10\,000$ m; and $R_1=R_2=15\%$ at $z=15\,000$ m. (Note that at the time when moisture is added, the surface front is centered at $x=500$ km and is moving toward the more humid air mass.)

In addition, the boundary conditions on the lower boundary have been modified to simulate the effects of daytime diurnal heating:

1) Surface heating Q is initiated at the time $t=t_H=6$ h (1 h after moisture is added) with

$$Q=Q_D\sin[\pi(t-t_H)/t_D]$$

with $t_D=12$ h. This heating is designed to simulate the daytime heating of the atmosphere near the ground by sensible and latent heat flux. No radiative transfer within the atmosphere is explicitly incorporated and no shading of the surface by clouds is considered. Also, nighttime cooling is not included so that the surface is adiabatic after "sunset."

2) In order to roughly simulate the addition of moisture from the surface to the atmosphere, the relative humidity of the air at the surface is fixed at its initial value until four hours after heating was initiated, at which time the surface moisture flux is set to zero by requiring that $q_z|_{z=0}=0$.

Solutions for $\Delta\theta_I=0°$, 4° and 8°C were obtained for the configuration described above. The potential temperature field was perturbed over the lower 1500 m every 900 s with a random number field over the range ± 0.1°C. Eddy viscosity parameters were chosen as $\kappa_0=1.\text{m}^2\ \text{s}^{-1}$ and $C=3.0$ so as to produce a well-mixed turbulent layer below the inversion. Finally, because of the unrealistically slow development of cloud systems in the present model (this slow development is apparently due to horizontal smoothing and to the model's coarse horizontal resolution which reduces vertical velocities by more than an order of magnitude compared to realistic values), the maximum surface heat flux Q_D was chosen to be 1400 W m^{-2}. This large value (5–10 times larger than typical observed values) was found to be necessary if the model was to produce deep convection within the 12 h heating period.

As heat is added to the surface layer in each case, an unstable convective layer develops at the surface and diffuses upward into the atmosphere. In the case $\Delta\theta_I=0$, this layer grows unimpeded by an inversion layer and produces convective clouds as the air saturates and is lifted further by randomly generated plumes. On the other hand, the presence of a temperature inversion will delay cloud formation since a portion of the surface heat input must be used to destroy the inversion before condensed air parcels may be lifted to the level of free convection.

At the same time as the surface heating is acting, the frontal system is moving from the left toward the moist air mass with the frontal circulation (similar to that shown in Fig. 11) acting upon the moisture field. The initial position of the front has been chosen so that surface heating will trigger deep convection before frontal lifting in the case $\Delta\theta_I=0°$. Hence the first vertical velocity maximum ($w_{\max}=6.6$ m s^{-1}) in the case $\Delta\theta_I=0°$ occurs some 500 km ahead of the front at $x=1200$ km at the time $t=16$ h (or $t_H+10.0$ h). As the top frame of Fig. 12 shows, this maximum is the strongest of four updraft zones with the two cloud systems adjacent to the most intense cloud suppressed by the subsiding air surrounding it. The large cloud system near the front at $x=920$ km achieves a vertical velocity peak of similar intensity at 16.2 h. The low-level cloud zone immediately above the front at 700 km does not develop into a convective cloud, apparently having been suppressed by the large cloud downwind and by more stable moisture-temperature conditions along the frontal surface.

When an inversion of intensity $\Delta\theta_I=4$°C is added to the solution, the occurrence of the first velocity peak is delayed until 19.6 h with this peak ($w_{\max}=4.4$ m s^{-1}) at $x=1400$ km triggered by surface heating (middle frame of Fig. 12). A second peak ($w_{\max}=4.6$ m s^{-1}) appears at $x=940$ km at $t=20.2$ h; as before, this second cloud system is apparently produced by the frontal circulation.

Finally, when the most intense inversion $\Delta\theta_I=8$°C is used, the first vertical velocity peak ($w_{\max}=3.8$ m s^{-1}) is delayed until $t=24.8$ h as the bottom frame of Fig. 12 shows.[2] The strong inversion prevents moist convection by surface heating alone as shown by the stable cloud

[2] In both this and the previous inversion cases, deep convection does not occur until after "sunset" (18 h). Because nighttime radiative cooling is not present in the model, the lower atmosphere of the model should be more unstable than it would be if cooling were present. Hence the development of deep convection in the case $\Delta\theta_I=8$°C at 6.8 h after "sunset" might be delayed or prevented by nocturnal cooling.

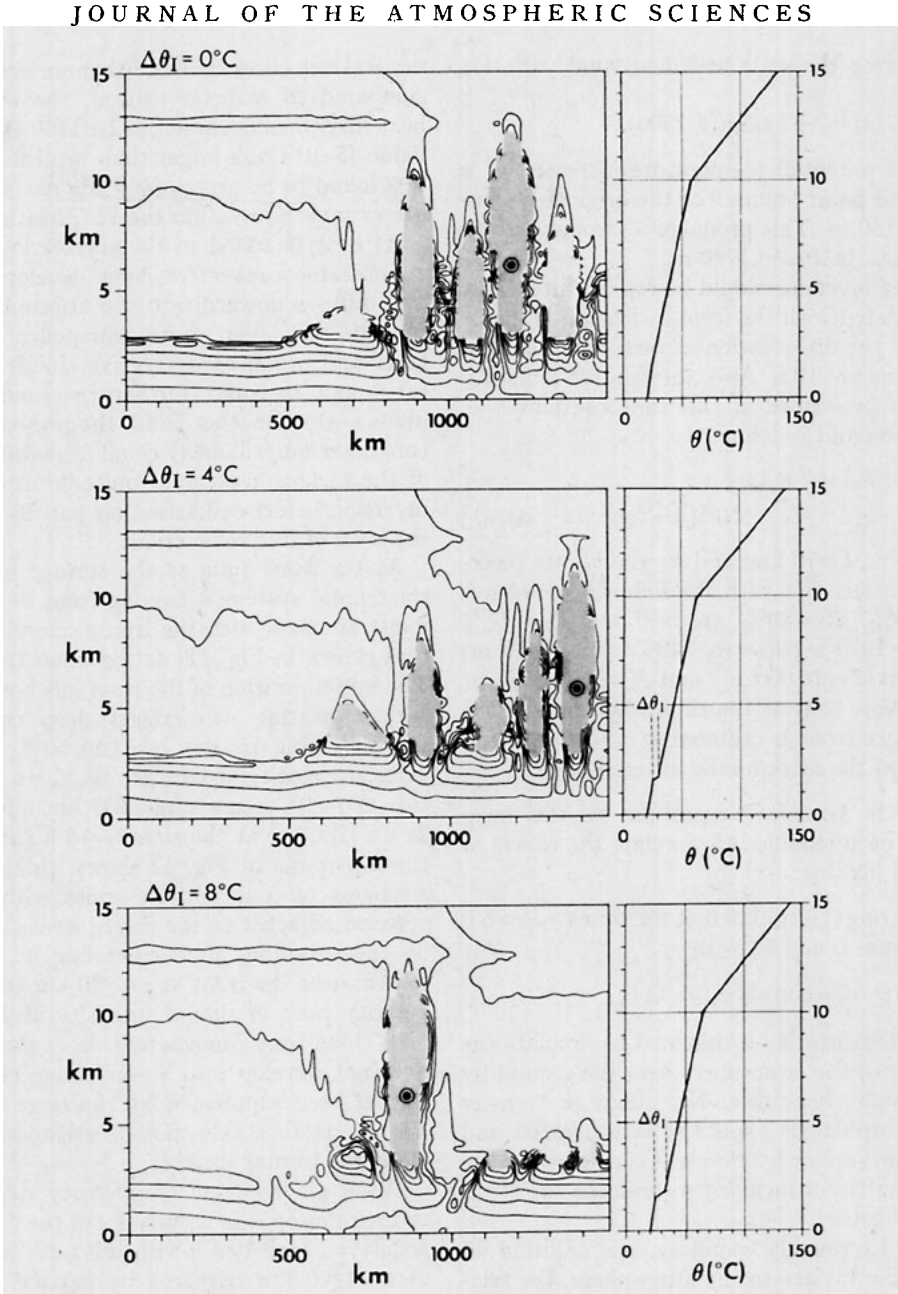

FIG. 12. Composite plots showing fields of relative humidity (contours) and condensed water (shaded region) for the three solutions described in the text for different potential temperature jumps $\Delta\theta_I$. Each frame shows conditions in the solution at the time of maximum vertical velocity (the location of which is marked by a bulls-eye): $t=15.97$ h for $\Delta\theta_I=0°C$, $t=19.55$ h for $\Delta\theta_I=4°C$, and $t=24.80$ h for $\Delta\theta_I=8°C$. The graph to the right of each plot shows the initial potential temperature profile on the warm air side of the front. The contour interval for relative humidity is 10%.

water regions near the height of the inversion downwind of the convective cloud. Hence frontal lifting is now essential to the generation of the deep convection in this case; in fact, because intense lifting is required, the cloud formation has been delayed until the maximum vertical velocity in the frontal circulation reaches the moist air mass.

As indicated by the results of the above three experiments, the timing of the arrival of the front at the moist air mass relative to the time t_H is an important factor in determining the evolution of moist convection in the model. In order to demonstrate this, three new solutions were obtained which are identical to the above cases except that the starting time t_H for surface heating

was changed from 6 h to 13 h. Because of this seven-hour delay in the heating, the first velocity peak in all three cases now is found to occur adjacent to the front with the times of occurrence relative to t_H reduced by several hours in each case: $t-t_H=8.4$, 10.7 and 15.4 h for $\Delta\theta_I=0$, 4 and 8°C, respectively. Also the vertical velocity maxima increased considerably relative to their previous values with $w_{\max}=7.3$, 6.8 and 4.8 m s^{-1} for $\Delta\theta_I=0$, 4 and 8°C, respectively. Hence the frontal circulation was found to produce the most intense convection when it is able to act upon the moist air before surface heating can produce convection and thereby reduce the instability of the moist surface layer.

Before concluding this discussion, we must point out that the method of producing free convection in the heated surface layer by means of random temperature perturbations is somewhat inadequate in the present model because of the coarse horizontal resolution. The effect of this procedure is to generate buoyant elements of width Δx or 20 km whereas actual elements will be on the order of 100 meters. These unrealistic thermals in the model are then able to penetrate the capping inversion with little entrainment weakening and to trigger deep convection with an intensity similar to that produced by the properly resolved frontal lifting. On the other hand, the actual smaller thermals would have much more difficulty in penetrating the capping inversion and, if they did manage to pass through the inversion, would produce cumulus clouds of much smaller diameter which would be far more subject to weakening through entrainment. Hence the moist convection produced by surface heating in the model may be excessively intense when compared with the convection generated in the frontal system.

6. Summary of results

A study has been made of the effect of moisture upon the cross-stream frontal circulation which Orlanski and Ross (1977) have investigated in idealized dry frontal systems. In the moist numerical solutions obtained here, the dynamics of the frontal circulation were resolved by the model while cumulus convection was treated on the grid scale using an eddy viscosity which gradually adjusted the unstable saturated air to a neutral state as the convection developed.

The results of this study can be summarized as follows:

1) The initial presence of unsaturated water vapor in the dry solution was shown to have little effect upon the frontal circulation. However, as vertical motion within the frontal system produced saturation, latent heat release produced changes in the frontal system which depended upon the location and intensity of the lifting and the degree of convective instability in the warm air mass ahead of the advancing cold front.

The most intense upward motion in the dry surface jet case occurred in the stable cold air mass upwind of the front; therefore the frontal circulation in this case initially produced only stable clouds behind the front. The much weaker lifting of a secondary circulation cell above the nose of the front produced an unstable convective zone in the warm air mass some eight hours after moisture was added.

In the midtropospheric jet case, the strongest circulation cell within the front was located so as to produce strong lifting in the warm air immediately above the front. Therefore unstable convection began much earlier in this case with free convection occurring approximately 2 h after a relative humidity field identical to that used in the surface jet case was added to the dry solution.

2) As the moist convection developed, the vertical motion within the zone increased to a maximum intensity and then decreased as the top of the cloud-water region approached the tropopause. The convection-induced circulation completely overshadowed the original frontal circulation well before the time of peak updraft intensity.

3) The initial growth of the convective zone in the midtropospheric jet case was shown to excite a gravity wave with horizontal and vertical scales equivalent to those of the convection region. This gravity wave propagated into the warm air at a much faster speed than the moving front-cloud system. Gravity waves similar to the one produced in this case have been observed to trigger new convection far from the point where the waves were generated.

4) Comparisons of solutions using different initial humidity conditions indicated that parcel lifting alone was sufficient to achieve saturation in the model with diffusion effects unimportant. However, after saturation occurred in moist unstable regions, diffusion resulting from the nonlinear eddy viscosity was shown to be as important as vertical velocity in the further development of the convective zone in the model. The development of this convection was still much slower than is observed in nature because the maximum updraft velocity permitted in the model consists of a value averaged over Δx (20 km).

5) As expected, a reduction of the initial humidity levels in the lowest two kilometers of the model reduced the ultimate intensity of the convection because of the lower convective instability of the atmosphere and the reduced moisture supply available to the moist convection. On the other hand, a large reduction of the relative humidity in the ambient air above two kilometers only reduced the convective intensity slightly with this reduction apparently caused by the entrainment of drier air into the cloud zone. Also a lowering of the overall temperature by 10°C reduced the convective activity drastically by stabilizing the atmosphere.

6) A set of solutions was obtained in which the initial conditions included a capping inversion as a potential temperature jump $\Delta\theta_I$ at a height of about 2 km.

Comparison of these results shows the convective intensity, as indicated by maximum vertical velocity, to be inversely proportional to the jump magnitude $\Delta\theta_I$.

7) In order to model atmospheric conditions which are more representative of actual frontal initiation of severe storms, we have produced a set of solutions in which the magnitude $\Delta\theta_I$ of a low-level capping inversion was varied from 0 to 8°C for the case of a dry front overtaking a moist air mass with diurnally varying surface heating included. When no inversion was present, the surface heating was found to produce convection before the front could affect the moist air. However, as the inversion jump $\Delta\theta_I$ was increased, triggering due to surface heating was suppressed, and frontal lifting was needed in addition to diurnal heating in order to produce convection. Because of the coarse model resolution, the convection triggered by diurnal heating in the case without an inversion is nearly as intense as that produced by the frontal lifting. However, one may infer that, in the real atmosphere, such heat-triggered convection will consist of small-scale cumulus clouds which will be more easily eroded by entrainment than will those produced by the more organized frontal lifting. Hence the tendency of the inversion to prevent the release of the moist instability by small-scale heated plumes permits the frontal lifting to produce moist convection which exhibits a broader scale and which may therefore develop into a more intense storm.

APPENDIX

Comparison of Solutions With and Without the Hydrostatic Approximation

A set of three solutions of the surface jet configuration was produced in order to determine the effect of different forms of the vorticity-streamfunction relation [Eqs. (2.3) and (2.4)] upon a typical moist front solution. The model used in this comparison is identical to that used in the basic moist solution SJ3 of Section 3 except that the vertical grid spacing Δz was held constant at a value of 200 m (a typical value in the lower troposphere of the stretched-coordinate solution of Section 3) in order to facilitate the solution of the elliptic equation (2.3). Since there are 51 points in the vertical, the rigid lid boundary is thus lowered from the original height of 15 000 to 10 000 m in the present solutions.

Three solutions will be compared here. In the first or anelastic solution, the exact expression

$$\alpha_0\frac{\partial^2\psi}{\partial x^2}+\frac{\partial}{\partial z}\left(\alpha_0\frac{\partial\psi}{\partial z}\right)=\zeta,$$

which is Eq. (2.3), is used to relate streamfunction and vorticity. Because this equation is elliptic for the unknown quantity ψ, it was solved iteratively in the model using an alternating-direction-implicit or ADI method (see Young, 1971). In the second solution, referred to as the hydrostatic case, the hydrostatic approximation is made to produce Eq. (2.4), i.e.,

$$\frac{\partial}{\partial z}\left(\alpha_0\frac{\partial\psi}{\partial z}\right)=\zeta.$$

Finally, in the third or filtered hydrostatic case, the hydrostatic streamfunction is smoothed in the horizontal using a filtering expression which is one form of

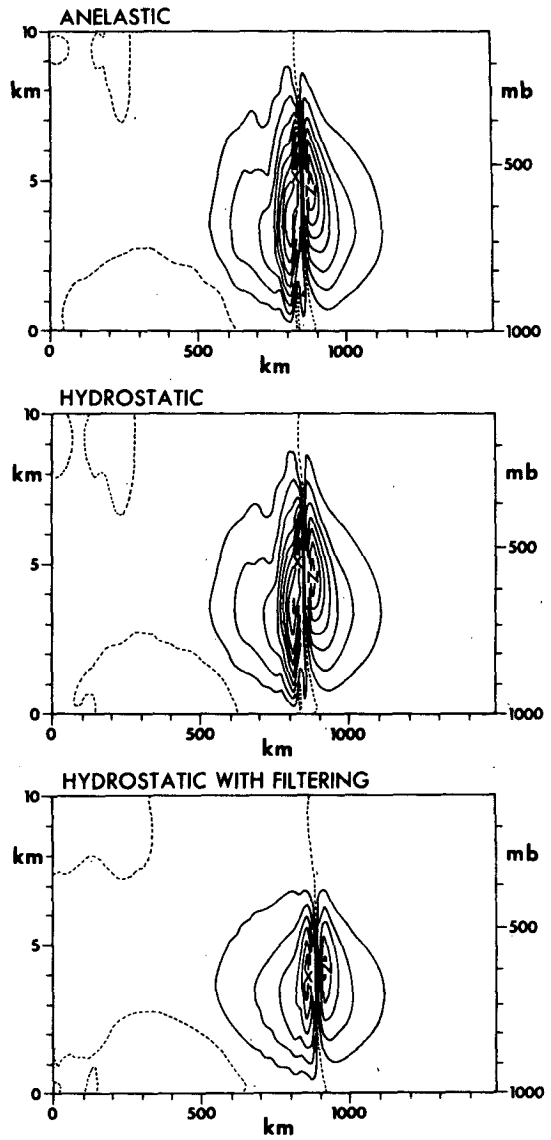

FIG. 13. Plots of perturbation streamfunction ψ' at time $t=30.20$ h from the three surface jet solutions described in the Appendix. The symbols X and N denote, respectively, the maximum and minimum ψ': 18 290 and −15 090 kg (m s)$^{-1}$ for the anelastic case; 19 380 and −15 080 kg (m s)$^{-1}$ for the hydrostatic case; 13 310 and −10 480 kg (m s)$^{-1}$ for the hydrostatic case with filtering. Contour interval $\Delta\psi'$ is 2000 kg (m s)$^{-1}$.

Shuman's (1957) 3-point smoothing method:

$$\psi_{I,J}=0.25\psi^{\text{hydro}}_{I+1,J}+0.50\psi^{\text{hydro}}_{I,J}+0.25\psi^{\text{hydro}}_{I-1,J}$$

where ψ^{hydro} is the streamfunction obtained from the hydrostatic equation (2.4) and the subscripts I and J refer to respective x and z grid locations. Smoothing was done in this third solution in order to reduce the high-wavenumber gravity-wave noise associated with the deep convection in the moist solution.

All three solutions were run until the convective zone reached the vicinity of the top boundary. At the time when the unstable convection first appears, all three solutions are nearly identical. However, as the convection intensifies and the horizontal gradients of streamfunction increase, the filtered solution begins to diverge from the two unfiltered cases as one might expect.

Fig. 13 shows a comparison of the three streamfunction fields at the time $t=30.2$ h when the vertical velocity is approaching its maximum value. The hydrostatic and anelastic solutions are very similar to the streamfunction maxima differing by only 6%. The maximum in the filtered solution is 30% smaller than that of the other two cases with the vertical velocity reduced by 60% at this time. On the other hand, the filtering of high wavenumber noise is evident in the lower frame of Fig. 13. Also, a comparison of the vertical velocity time histories of the three cases indicates that the filtering causes the velocity peak to be delayed two hours with the maximum value being reduced by 25% from the unfiltered value.

Given the fact that convection dynamics is only crudely represented by the model, the changes produced by the filtering are not considered to be significant.

Acknowledgments. The authors are very grateful to Drs. Kikuro Miyakoda and Frank Lipps for their help in clarifying the manuscript and to Mr. Larry Polinsky for his programming assistance with the computer graphics routines. We also appreciate the excellent job done by Mrs. Joyce Stintsman in typing the manuscript and by members of the GFDL drafting group in preparing the figures.

REFERENCES

Asai, T., 1962: Numerical experiment of convection in the model atmosphere. *Proc. Int. Sym. Numerical Weather Prediction*, Tokyo, Meteor. Soc. Japan, 469–476.

Beebe, R. G., and F. C. Bates, 1955: A mechanism for assisting in the release of convective instability. *Mon. Wea. Rev.*, **83**, 1–10.

Bosart, L. F., and J. P. Cussens, Jr., 1973: Gravity wave phenomena accompanying east coast cyclogenesis. *Mon. Wea. Rev.*, **101**, 446–454.

Brunk, I. W., 1949: The pressure pulsation of 11 April 1944. *J. Meteor.*, **6**, 181–187.

Cornelius, C. J., Jr., D. F. Glevy and R. T. Williams, 1975: The inclusion of moisture in a numerical model of steady state fronts. Tech. Rep. NPS-51Wu75051, Naval Postgraduate School, Monterey, Calif., 74 pp.

Fawbush, E. J., and R. C. Miller, 1953: A method for forecasting hailstone size at the earth's surface. *Bull. Amer. Meteor. Soc.*, **34**, 235–244.

Fulks, J. R., 1951: The instability line. *Compendium of Meteorology*, Amer. Meteor. Soc., 647–652.

Lipps, F. B., 1977: A study of turbulence parameterization in a cloud model. *J. Atmos. Sci.*, **34**, 1751–1772.

Manabe, S., J. Smagorinsky and R. F. Strickler, 1965: Simulated climatology of a general circulation model with a hydrologic cycle. *Mon. Wea. Rev.*, **93**, 769–798.

Miyakoda, K., J. Smagorinsky, R. F. Strickler and G. D. Hembree, 1969: Experimental extended predictions with a nine-level hemispheric model. *Mon. Wea. Rev.*, **97**, 1–76.

Newton, C. W., 1950: Structure and mechanism of the prefrontal squall line. *J. Meteor.*, **7**, 210–222.

Ogura, Y., and N. A. Phillips, 1962: Scale analysis of deep and shallow convection in the atmosphere. *J. Atmos. Sci.*, **19**, 173–179.

Orlanski, I., and B. B. Ross, 1973: Numerical simulation of the generation and breaking of internal gravity waves. *J. Geophys. Res.*, **78**, 8808–8826.

——, and ——, 1977: The circulation associated with a cold front. Part I: dry case. *J. Atmos. Sci.*, **34**, 1619–1633.

Showalter, A. K., 1953: A stability index for thunderstorm forecasting. *Bull. Amer. Meteor. Soc.*, **34**, 250–252.

Shuman, F. G., 1957: Numerical methods in weather prediction: II. Smoothing and filtering. *Mon. Wea. Rev.*, **85**, 357–361.

Smagorinsky, J., 1960: On the dynamical prediction of large-scale condensation by numerical methods. *Geophys. Monogr.*, No. 5, Amer. Geophys. Union, 71–78.

Takeda, T., 1965: The downdraft in convective shower-cloud under the vertical wind shear and its significance for the maintenance of convective system. *J. Meteor. Soc. Japan*, **43**, 302–309.

——, 1971: Numerical simulation of a precipitating convective cloud: The formation of a "long lasting" cloud. *J. Atmos. Sci.*, **28**, 350–376.

Uccellini, L. W., 1975: A case study of apparent gravity wave initiation of severe convective storms. *Mon. Wea. Rev.*, **103**, 497–513.

Williams, R. T., 1974: Numerical simulation of steady state fronts. *J. Atmos. Sci.*, **31**, 1286–1296.

Young, D., 1971: *Iterative Solution of Large Linear Systems*. Academic Press, 570 pp.